Atom Probe Tomography Study of Multi-microalloyed Carbide and Carbo-Nitride Precipitates and the Precipitation Sequence in Nb-Ti HSLA Steels

MONICA KAPOOR, RONALD O'MALLEY, and GREGORY B. THOMPSON

Composition analysis of carbide and carbo-nitride precipitates was performed for two Nb-Ti microalloyed steels with yield strengths of 750 and 580 MPa using an atom probe study. In the high-Ti 750 MPa steel, Ti-rich (Ti,Nb)(C,N) and Ti-rich (Ti,Nb)(C) precipitates were observed. In the high-Nb 580 MPa steel, a Ti-rich (Ti,Nb)(C,N) precipitate and (Ti,Nb)(C) clusters were noted. These (Ti,Nb)(C) clusters in the high-Nb 580 MPa steel were smaller than the (Ti,Nb)(C) precipitates in high-Ti 750 MPa steel. In general, a larger number of precipitates were found in the high-Ti 750 MPa steel. This difference in the number density of the precipitates between the two steels is attributed to the difference in Ti content. Combining the atom probe tomography results and thermodynamic calculations, the precipitation sequence in these alloys was inferred to be the following: as the temperature decreases, TiN precipitates out of the solution with successive (Ti,Nb)(C,N) layers of varying composition forming on these Ti-rich precipitates. Once N is depleted from the solution, a second set of (Ti,Nb)(C) precipitates in a similar manner in the matrix and also onto the carbo-nitride phase. This observation is consistent with previous observations in high-strength low-alloy steels containing comparable amounts of only Nb. It was noted that the amount of Nb, Nb/(Nb + Ti), in the precipitates decreased from 0.20 to 0.04 with the size of the precipitate. We believe that this is due to the Nb supersaturation in the matrix when these precipitates nucleate.

DOI: 10.1007/s11661-016-3398-6

I. INTRODUCTION

MICROALLOYED steels use a combination of grain size refinement, microstructure control, and precipitation strengthening, *via* microalloying with elements such as Ti, Nb, V, and Mo, to obtain an optimal combination of strength and toughness.[1–8] The combination of these microalloying elements with interstitial solutes, such as C and N, leads to the formation of carbides, nitrides, and complex carbo-nitrides.[7,9–13] In general, Ti, Nb, and V facilitate grain refinement through precipitation in the austenite and contribute to dispersion hardening through carbide precipitation in ferrite. Nb can retard recovery and recrystallization during hot rolling resulting in ferrite grain refinement, and Ti combines with nitrogen to form TiN precipitates at high temperature in austenite which prevent grain growth.[1] In contrast, V contributes more to precipitation strengthening because it has a low solubility in ferrite and precipitates readily at lower temperatures.[1,2] The relative contribution of microalloying elements is determined by the solubility of their carbide/nitride/carbo-nitride phases in the microstructure.

In the innovative mini-mill process used to make thin slabs, lower temperatures and short reheating times are employed.[12] This limits the amount of elements that can be added and held in solution to be precipitated for microstructure control. So, multiple strengthening mechanisms, using various elements, need to be employed to achieve strength levels that are comparable to those that can be achieved with single-element microalloy systems and long high-temperature slab soaking times.

Combining microalloy systems can result in synergistic behaviors resulting in steels that exhibit very high strength levels, low rolling loads, and also good impact toughness. However, interaction of multiple elements can effect precipitation behavior of each element and not necessarily result in additive strengthening mechanisms, thereby effecting the mechanical properties of the steel.[9,11–13] For instance, addition of Ti to V-N microalloyed steels can decrease the yield strength as a result of preferential formation of TiN precipitates at higher temperatures in austenite.[14] The V-Ti-N precipitates forming at a higher temperature reduce the amount of V and N available for subsequent precipitation at low temperatures in ferrite.[15] This reduces the volume fraction of precipitates available for strengthening resulting in a decrease in yield strength. Similarly,

MONICA KAPOOR, formerly Postdoctoral Fellow with the Department of Metallurgical and Materials Engineering, The University of Alabama, Tuscaloosa, AL, is now ORISE Postdoctoral Fellow with National Energy Technology Laboratory, Albany, OR 97321. GREGORY B THOMPSON, Professor, is with the Department of Metallurgical and Materials Engineering, The University of Alabama. Contact e-mail: gthompson@eng.ua.edu RONALD O'MALLEY, formerly Plant Metallurgist with Nucor Steel Decatur, LLC, 4301 Iverson Blvd., Trinity, AL 35673, is now F. Kenneth Iverson Chair Professor and Director with PSMRC, Materials Science and Engineering, Missouri S&T, 284 McNutt Hall, 1400 N. Bishop Ave., Rolla, MO 65409-0340.

Manuscript submitted March 30, 2015.
Article published online March 2, 2016

compact-strip-processed Ti-Nb alloyed steels sometimes form star-shaped (Ti,Nb)(C,N) precipitates, which are NbC-rich precipitates co-precipitating on a core of TiN.[8,15,16] This depletes the matrix of Nb at a higher temperature, which would otherwise have been used in grain refining or for subsequent strengthening in the ferrite at low temperature.[15] To add to the complexity, similar systems with small variations in composition can result in steels with different microstructures and/or mechanical properties.[17] For instance, addition of only 0.08 wt pct Nb altered the austenite–ferrite transformation temperature, thereby the microstructure resulting in ~30 pct increase in yield strength.[17,18] This brief overview illustrates how the type and amount of alloying elements control the mechanical properties in multi-microalloy steel through microstructure control and precipitation.

Most of the studies investigate the effect of processing parameters and bulk composition on the formation of these precipitates[8,12,14,19] and use transmission electron microscopy (TEM), energy-dispersive X-ray spectroscopy (EDS), and electron energy loss spectroscopy (EELS) to report the composition of the precipitates.[3,13,20–24] EDS can provide enrichment details but lacks in accurate quantitative information at the nanoscale, as needed for studying these precipitates. For instance, EDS could not preclude the possibility of elemental enrichment at carbo-nitride precipitate/matrix interfaces.[25] In contrast, atom probe tomography (APT) could provide the spatial and composition resolution needed for such analysis. Most of the earlier atom probe studies have focused on precipitation in single microalloy systems with an emphasis on Nb-based steels.[26,27] There are atom probe studies on clustering and interphase precipitation but very few on the precipitate composition in multi-microalloy systems.[17,25,28] The challenges of such a study lie in the small size, low number density, and the variety of structurally similar precipitates having different compositions.

Jia *et al*. studied a multi-microalloyed Nb-Ti steel and inferred the formation of mutually cross-soluble (Ti,Nb)(C) precipitates based on lattice parameters obtained by electron diffraction.[13] For a detailed TEM analysis, the readers are referred to this study. However, the composition of these cross-soluble precipitates has yet to be studied by APT, which can provide accurate compositions as well as the spatial distribution of the elements within the precipitate. Such information links the processing to the interaction of multiple elements and their individual solubility and precipitation behavior. For example, the addition of 0.036 wt pct Ti to Nb-based hot-rolled steel makes it easier to precipitate out Nb as (Ti,Nb)(C), resulting in better grain refinement.[22] In another steel studied by Wang *et al*., the addition of Ti to compact-strip-processed Ti-Nb alloyed steels leads to easier formation of (Ti,Nb)(C,N) precipitates with Nb-rich portions.[15] Unfortunately, these Nb-rich portions trap Nb making it less available for subsequent grain refinement and interphase precipitation detrimentally effecting the mechanical properties.[15] Therefore, addition of Ti and its subsequent interaction with Nb result in enhanced grain refinement in one steel and suppressed grain refinement in the other steel. By employing APT to determine the morphology, size, and composition of multi-microalloyed carbide and carbo-nitride precipitates formed in steels, subtle details associated with their size and composition can be revealed and can help us understand Ti-Nb interaction in these steels.

In this APT-focused work on Ti-Nb high-strength low-alloy (HSLA) steels, we study how the presence of multiple microalloying elements affects the precipitate compositions. Based on these experimental results, we use thermodynamic calculations to reconstruct the precipitation sequence, the solute distribution, and its effect on precipitation events in the Ti-Nb multi-microalloyed steels which would be difficult, if not impossible, to achieve experimentally in these industrial trial steels.

II. EXPERIMENTAL PROCEDURES

Chemical compositions of two HSLA steels, with yield strengths of 750 and 580 MPa, are presented in Table I. Designations of alloy 1 and alloy 2, respectively, are used throughout this discussion. Both alloy 1 and alloy 2 exhibit ferritic microstructures as confirmed by X-ray diffraction, Fig. S1. Grain size was in the range of 2 to 4 μm for both the alloys, confirmed by ion contrast imaging, Fig. S2. The total (Ti + Nb) concentration is 0.16 and 0.10 at. pct in alloy 1 and 2, respectively. This (Ti + Nb) concentration is an order of magnitude larger than V (0.015 and 0.004 at. pct in alloy 1 and 2, respectively), which is known to form mixed (Ti,Nb,V)(C,N) precipitates in similar systems.[1] Subsequent Thermo-Calc® results show that Ti and Nb are the primary contributors to the observed microalloyed precipitation trends in our carbides and carbo-nitrides; consequently, they are the elements of primary focus in this paper.

Alloy 1 and alloy 2 were made using the direct hot charge thin-slab casting process. They were produced as industrial trial heats at Nucor Steel, Decatur, AL—continuously cast as 90-mm (3.5 in.) thick slabs which are directly hot charged to the hot mill through a furnace at 1523 K (1250 °C) and subsequently hot rolled to the final thickness, 2 mm (0.080 in.) and 9.25 mm (0.375 in.). The strips were then finish-rolled at 1158 K (885 °C), cooled rapidly to 894 K (621 °C) by laminar cooling, and then allowed to slow cool (60 ± 20 °C/s) to room temperature from 894 K (621 °C) in coil form.

TEM studies were performed using a 200 KeV field emission FEI TECNAI (scanning) transmission electron microscope (STEM) with an annular dark-field detector which permits high-angle annular dark-field (HAADF) imaging. The TEM specimens, approximately 6 to 7 μm × 1 μm in cross-section, were prepared using a lift-out and thinning procedure with 30 KV beam energy at currents ranging from 0.3 to 0.5 nA. A clean-up step was performed to remove the surface damage due to Ga ion implantation with 5 KV beam energy and 70 pA current.

APT studies were conducted using a Cameca Local Electrode Atom Probe (LEAP®) 3000XSi. APT tip

Table I. Chemical Compositions of the Experimental Alloys Studied

	C	Si	Mn	Ti	Nb	V	N	Fe
Alloy 1								
(wt pct)	0.050	0.300	1.280	0.116	0.034	0.014	0.009	Bal.
(at. pct)	0.231	0.593	1.294	0.135	0.020	0.015	0.036	Bal.
Alloy 2								
(wt pct)	0.040	0.220	1.030	0.060	0.060	0.004	0.008	Bal.
(at. pct)	0.185	0.436	1.043	0.069	0.034	0.004	0.032	Bal.

blanks (~1 μm diameter) were prepared using an FEI Quanta 200 3D Dual Beam™ scanning electron microscope/focused ion beam (SEM/FIB) microscope followed by annular ion milling for final sharpening into a needle-like specimen geometry. A low-energy clean-up step to reduce Ga ion implantation on the surface is also employed. The APT studies were conducted in laser mode with a pulse repetition rate of 200 kHz with a pulse energy of 0.2 to 0.4 nJ at 30 K (−243 °C) base temperature. The atom probe data were reconstructed using Image Visualization and Analysis Software (IVAS™) 3.6.6 package. The laser energy was set at 0.2 nJ in all runs except one, where 0.4 nJ energy was used. This altered the charge state ratio which necessitated a correction, using a combination of the isotope abundance ratio and peak decomposition function, applied to the proximity histogram to extract the carbon composition. This has been adapted from the work of Angersayd *et al.* on Ti(C,N).[29]

Approximately 20 tips (~300 millions ions collected) were studied for alloy 1 and 45 tips (~500 million ions collected) were studied for alloy 2. Each of these tips collected more than 5 millions ions and did not experience any peculiar field evaporation or significant reconstruction issues. The number density of the precipitates was calculated from the cumulative volume of the ranged ions in 20 tips for alloy 1 and 45 tips for alloy 2. Even though number density has limited validity, it is used as a normalized quantitative parameter to compare the number of precipitates per unit volume rather than using qualitative adjectives. The size of all the precipitates are based on full width at half maximum from the 1D composition profiles along the three axes or from proxigram composition profiles.[30] Similar reconstruction parameters have been used to reconstruct all the runs to ensure uniformity. This may result in some curvature at the top edges of the precipitates along the length of the tip (z axis). In all atom probe reconstructions, the blue, green, and red axes represent the z, y, and x axes, respectively, where z axis is the length of the tip (color available online). Clusters were identified using cluster analysis by the envelope method.[31] Nearest neighbor distances and minimum number of atoms to define a cluster were carefully determined to ensure minimizing the identification of random clusters.

Atom probe tomography analysis has a few inherent challenges—trajectory aberrations due to field evaporation differences, morphology reconstructions, surface migration and peak overlap in mass spectrum, *etc.* In this study, the reported compositions are from the core regions of the precipitates with minimum effect of trajectory aberrations.[32] Morphology reconstruction of these precipitates is an important topic which warrants detailed investigation and is beyond the scope of the present study. However, the general morphology characteristics of the precipitates and the clusters reported in this APT study are consistent with those reported in TEM studies of similar complex precipitates.[9,13,19,32] Inaccuracy in the C and N composition in the precipitates due to surface migration is not considered critical in this study because C and N will be bonded very strongly in the precipitates.[32,33] Last, unambiguous identification of Si and N which is complicated by the peak overlap in the mass spectrum is performed using a combination of isotope abundance ratios, and physical distribution of the species in the reconstruction. The details of the process are discussed in supplementary information along with a representative mass spectrum of alloy 1 and alloy 2, Fig. S3.

Equilibrium thermodynamic calculations were conducted using Thermo-Calc 3.1®, though the direct hot charge thin-slab casting process is not necessarily an equilibrium process. The intent of these calculations is to highlight the effect of Nb and Ti amounts on the trends and not necessarily to calculate absolute numbers. The calculations were carried out from 873 K to 1773 K (600 °C to 1500 °C) to understand how the precipitation sequence, the volume fraction of precipitates, and their composition are impacted by the multiple alloying elements of Nb and Ti.

III. RESULTS

TEM is the traditional precipitate analysis technique and we performed limited sampling of each alloy to compare and support precipitate size and distribution information obtained by APT. STEM–HAADF images of alloy 1, Figure 1(a), show the presence of numerous bright precipitates confirming the presence of a heavier element such as Nb in the precipitates. A close-up of one of the bright Nb-containing elliptical/cuboidal precipitate on the bottom left shows that the precipitate is approximately 20 nm in length and 10 nm in width. EDS of the precipitate indicated the presence of Nb. A similar image from alloy 2, Figure 1(b), shows no obvious Nb-containing precipitates in an area similar to that in alloy 1, approximately 6 to 7 μm^2. Multi-microalloyed Nb-Ti precipitates of similar non-equiaxed morphologies have routinely been observed in TEM studies[13] and are consistent with our STEM–HAADF images.

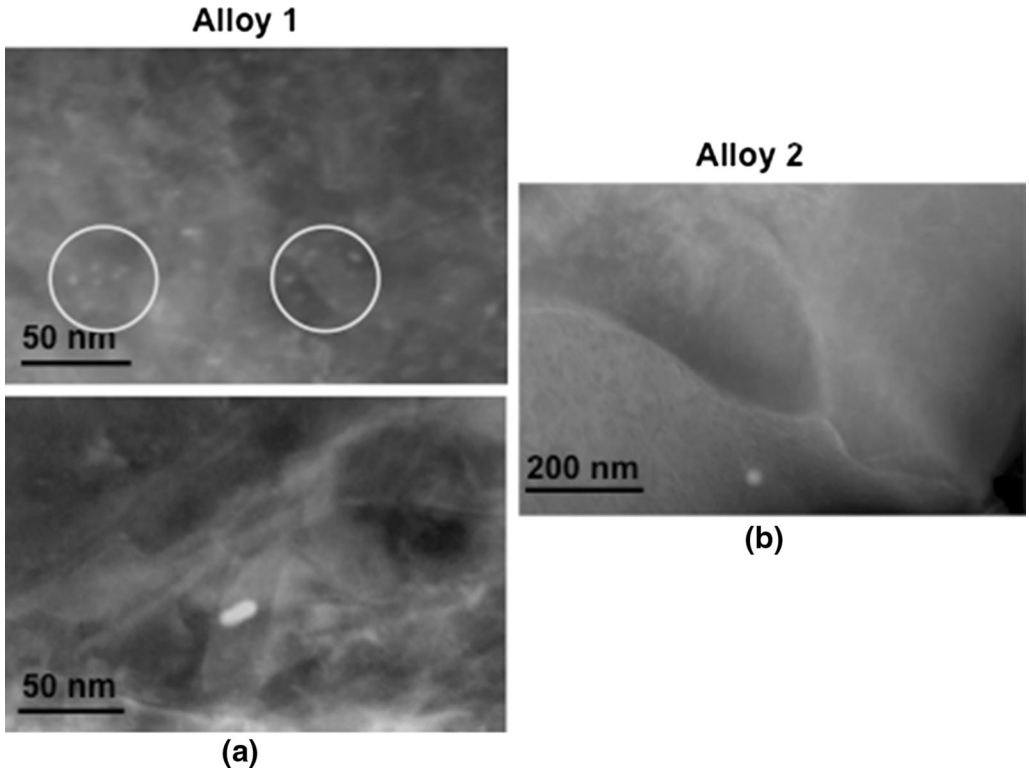

Fig. 1—STEM–HAADF images of (*a*) alloy 1 and (*b*) alloy 2. Alloy 1 has numerous bright precipitates, whereas alloy 2 does not show any precipitates. The bright spot in alloy 2 is due to beam damage.

Table II. Summary of Sampling in APT Study and the Size of Carbide and Carbo-Nitride Precipitates in Alloy 1 and Alloy 2 Obtained in APT Study

		Size (nm^3)	Figures
Alloy 1: total sampling volume—20 samples and 4.5×10^6 nm^3			
Carbide precipitate	(Ti,Nb)(C)-large	$16 \times 13 \times 8$	1(a)
	(Ti,Nb)(C)-medium	$7.5 \times 5 \times 5$	1(b)
	(Ti,Nb)(C)-small	1.5	1(c)
	(Ti,Nb)(C)-star	$70 \times 60 \times 30$*	4
Carbo-nitride precipitate	(Ti,Nb)(CN)	$40 \times 40 \times 10$	3
Alloy 2: total sampling volume—45 samples and 7.61×10^6 nm^3			
Carbo-nitride precipitate	(Ti,Nb)(C,N)	NA	5

*Dimensions of the portion observed, NA—a small portion of the precipitate was captured.

The focus of this investigation is to study the composition of the carbide and carbo-nitride precipitate phases in alloy 1 and alloy 2 using APT. We observed elliptical/cuboidal, spherical, and star-shaped/cruciform (Ti,Nb)(C) precipitates and elliptical/cuboidal (Ti,Nb)(C,N) precipitates in alloy 1 and a (Ti,Nb)(C,N) precipitate and (Ti,Nb)(C) GP-zone-like clusters in alloy 2. A summary of APT sampling statistics and precipitate morphology is provided in Table II.

A. *Carbide and Carbo-nitride Precipitates in Alloy 1*

Figures 2(a) through (c) show a series of 3D APT reconstructions with the (Ti,Nb)(C) precipitates formed in the 'high-Ti' alloy 1. The (Ti,Nb)(C) precipitates in Figures 2(a) through (c) are in different size ranges—approximately 16 nm × 13 nm × 8 nm cuboidal/elliptical, 7.5 nm × 5 nm × 5 nm cuboidal/elliptical, and 1.5-nm-radius spherical precipitates, respectively. These are designated (Ti,Nb)(C)-large, (Ti,Nb)(C)-medium, and (Ti,Nb)(C)-small, respectively, for the rest of the discussion.

Figures 2(d) through (f) show the corresponding proximity histograms of the precipitates, which is a 3D average composition profile as a function of distance from an isoconcentration surface, 5.5 at. pct Ti in this case.[30] The compositions in the core of the precipitate (all in at. pct) show that all (Ti,Nb)(C) precipitates are Ti-rich carbides with the details of the compositions in Table III. For (Ti,Nb)(C)-small, the core is considered to be the inner portion that has at least 100 detected ions. There are two results to note here. First, the

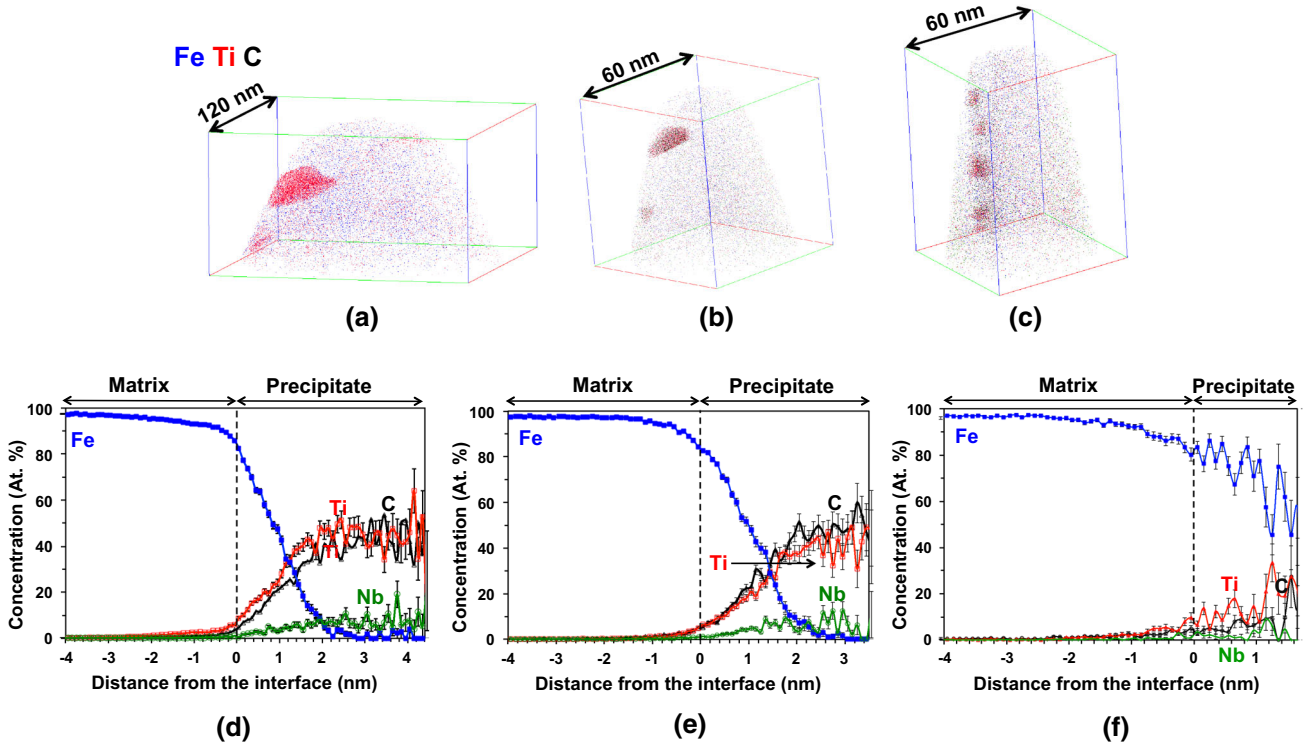

Fig. 2—(*a* through *c*) 3D atom probe tomography reconstructions showing various (Ti,Nb)(C) precipitates in alloy 1. Only a fraction of Fe atoms (blue dots) is shown. (*d* through *f*) Respective proximity histogram concentration profiles (at. pct) of Fe, Ti, Nb, and C for (Ti,Nb)(C) precipitates obtained from 5.5 at. pct Ti isoconcentration surface. The total number of detected ions in the precipitate portion of the proxigrams is 22826, 18494, and 1360, respectively. Color version available online.

Table III. Average Composition (At. Pct) of the Cores of the Precipitates in Alloy 1 as Measured by Atom Probe Tomography with the Proxigram Concentration Profile Method[30]

Carbide Precipitate	Composition
16 × 13 × 8 (nm^3) (Fig. 1a)	
Ti	44.39 ± 3.66
Nb	10.90 ± 2.30
C	42.39 ± 3.64
Fe	0
7.5 × 5 × 5 (nm^3) (Fig. 1b)	
Ti	43.35 ± 3.52
Nb	3.05 ± 1.22
C	51.59 ± 3.55
Fe	0
1.50 nm (Fig. 1c)	
Ti	31.58 ± 4.63
Nb	1.54 ± 1.23
C	22.18 ± 4.18
Fe	40.71 ± 4.88
Carbo-nitride precipitate	
40 × 40 × 10 (nm^3), Fig. 3	
Ti	40.26 ± 2.02
Nb	7.72 ± 1.10
C	48.24 ± 2.06
N	1.05 ± 0.42

The error for each concentration c is $\sigma = (c(1-c)/N)^{0.5}$, where N is the total number of detected ions used for calculating the concentration value.

amount of Nb in the (Ti,Nb)(C) precipitates decreased with the precipitate size—10.90 to 1.54 (at. pct) or 0.20 to 0.04 Nb/(Nb + Ti)—as the size decreased from approximately 16 nm × 13 nm × 18 nm to ~1.5 nm in radius. In addition, an absence of Nb was found in the inner 0.4 nm core (~30 detected ions) of the (Ti,Nb)(C)-small precipitate. The second observation was the presence of dissolved Fe in the (Ti,Nb)(C)-small precipitates. In contrast, no Fe was noted in the core of the (Ti,Nb)(C)-large and (Ti,Nb)(C)-medium precipitates. The dissolved Fe in the smaller precipitates is thought to be on the (Ti,Nb) sublattice, thereby lowering the lattice misfit and making it easier for the precipitates to nucleate, consistent with other experimental and computational studies.[26,34–39]

To highlight the absence of Nb in the 0.4 nm core of the (Ti,Nb)(C)-small precipitate, Figure 3(a) shows a 2D projection and 3D atom map of the smaller precipitate shown in Figure 2(c). Figure 3(b) is a close-up of the proxigram shown in Figure 2(f) with only Nb and Ti ions to illustrate that the core of the small precipitates is indeed Nb free. To delineate the Nb-free core, Ti and C ions are shown as smaller spheres (not to scale). The dependence of Nb in the precipitates on the precipitate size can be explained by the Nb supersaturation in the matrix when these precipitates nucleated. This will be addressed in detail in Section IV within the context of

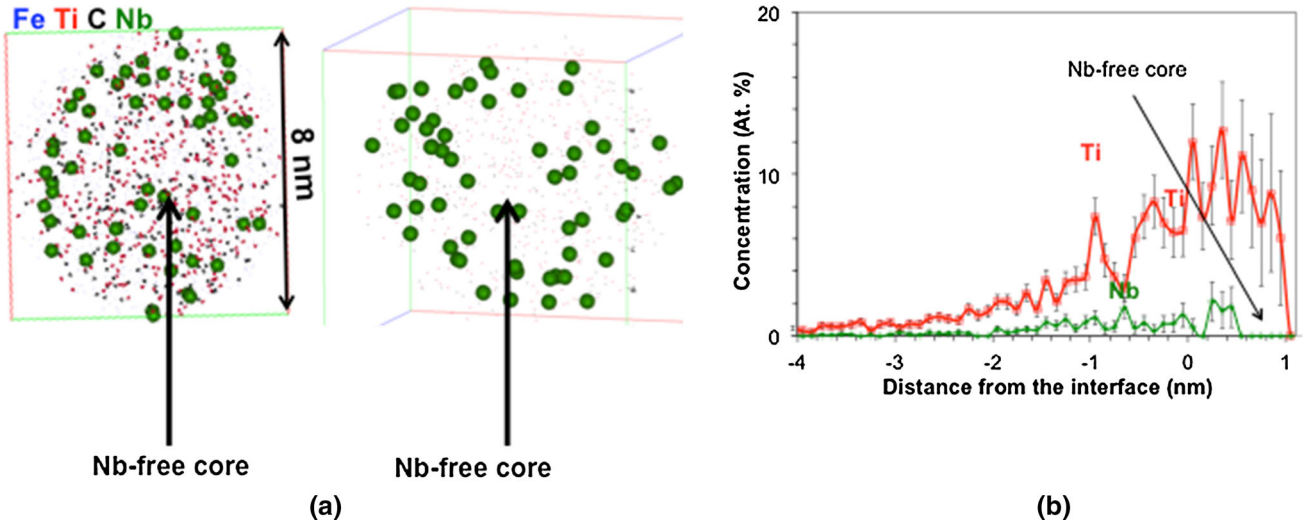

Fig. 3—(*a*) A close-up of (Ti,Nb)(C) precipitates illustrating the Nb-free core in the smaller precipitates in alloy 1, and (*b*) proximity histogram showing only Ti and Nb composition profile for clarity, with the Nb-free core labeled with the arrow. This view is along the length of the tip. The core region of the proxigram which shows no Nb has 400 detected ions in total. Ti and C atoms are not shown to scale in (a) and (b). The total number of detected ions in the precipitate portion of the proxigram is 1360. Color version available online.

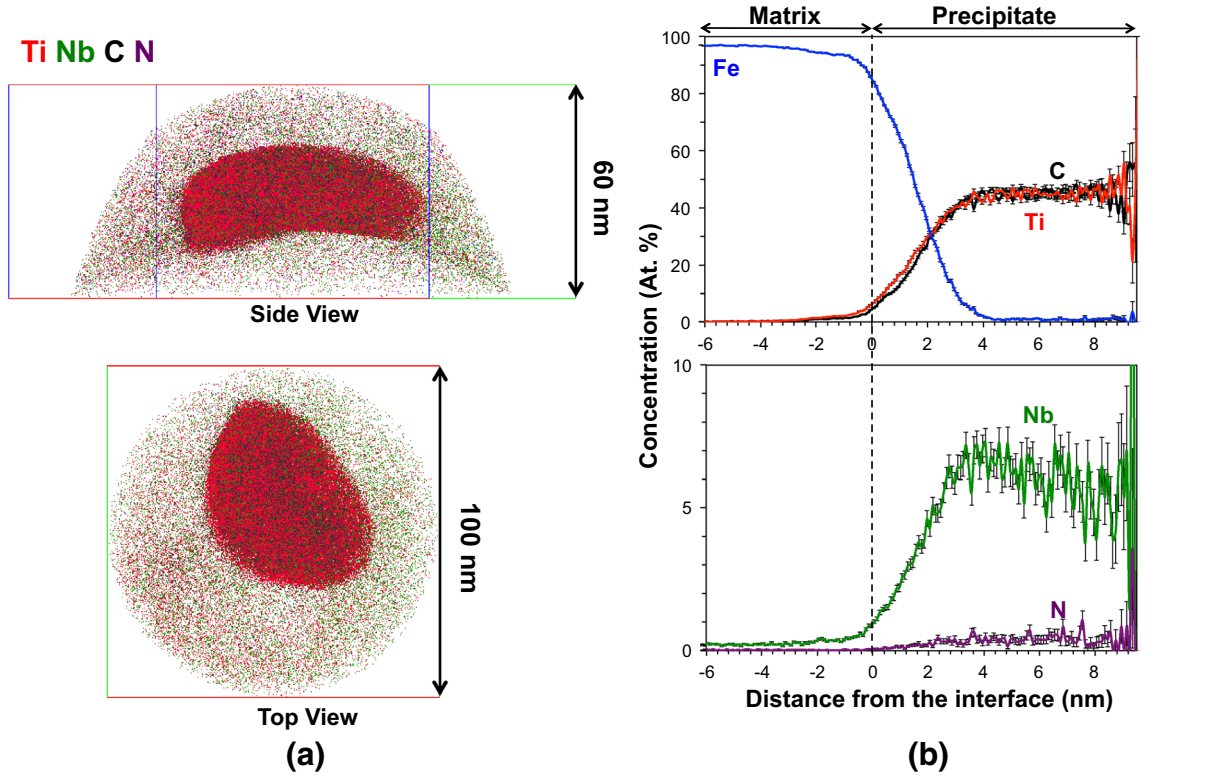

Fig. 4—(*a*) 3D APT reconstruction showing the top and the side view of a (Ti,Nb)(C,N) precipitate in alloy 1. (*b*) Proximity histogram concentration profiles (at. pct) of Fe, Ti, Nb, C, and N for (Ti,Nb)(C,N) precipitate obtained from 5.5 at. pct Ti isoconcentration surface. The total number of detected ions in the precipitate portion of the proxigram is 382,587. Color version available online.

the thermodynamic calculations. Analogous precipitation of a Ti-rich core followed by an NbC-rich shell has been observed in other studies[8,9,13,22] and also in steels with other alloying elements.[25]

Figure 4(a) is an atom map showing the top view and the side view and Figure 4(b) is the proximity histogram of the complex carbo-nitride precipitate, (Ti,Nb)(C,N), in alloy 1. The size of this precipitate is approximately 40 nm × 40 nm × 10 nm and its composition is 40.26 ± 2.02 Ti, 7.72 ± 1.10 Nb, 48.24 ± 2.06 C, and 1.05 ± 0.42 N (at. pct), Table III. Its size and composition can be explained by the nucleation temperature and the precipitation sequence of the alloying elements. Generally, the TiN precipitates out first at a higher

temperature followed by TiC.[1] As the temperature is lowered and supersaturation increases, NbN and NbC nucleate onto the precipitate already present, due to a lower activation energy barrier for nucleation. This precipitation sequence is also consistent with the larger size of the precipitate[19,40] because a precipitate that forms at a higher temperature will grow by acting as a nucleation site for the precipitates that will form at lower temperatures.

A portion of a 'star-shaped/cruciform' precipitate delineated by a 5.5 at. pct Ti isoconcentration surface is shown in Figure 5. To highlight the morphology of the precipitate, no other atomic species are shown in this figure. Based on the angle of the two sections, we infer that we are observing two arms of the 'star-shaped/cruciform' precipitate, ~70 nm × 60 nm × 30 nm in size, which has been seen in other TEM-based studies.[8,19] The size, composition, morphology, and formation temperature of these star-shaped/cruciform precipitates vary, but they are observed in steels containing Ti.[19] These precipitates are usually formed by a TiN/TiC-rich core precipitating out at a higher temperature in austenite.[8,19] As the temperature is lowered, supersaturation increases leading to epitaxial nucleation and growth of NbC at lower temperatures. The precipitates with star-shaped/cruciform morphology usually do not contribute to strength, but they do trap alloying elements which would otherwise be utilized in forming fine low-temperature precipitates that contribute to strengthening. The key result from our APT experimental observations is that this precipitate has ~17.05 ± 0.15 at. pct Nb or 0.26 Nb/(Nb + Ti), which is ~40 pct more Nb than that in other complex carbide precipitates, suggesting that these precipitates also retain Nb, reducing its amount available for subsequent low-temperature precipitation. The average composition of these precipitates is obtained based on the counts of Ti, Nb, and C encompassed within the precipitates and is listed in Table IV.

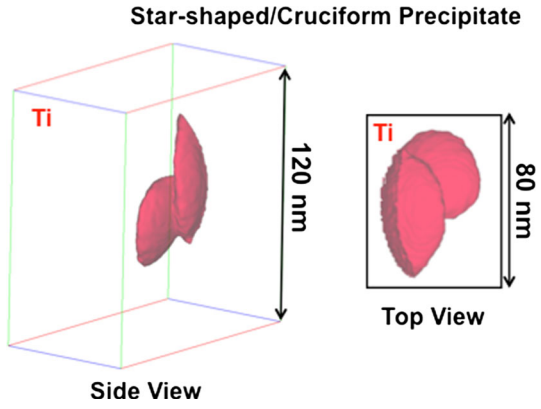

Fig. 5—Side view and top view of (Ti,Nb)(C) precipitate (red), delineated by a 5.5 At. Pct Ti isoconcentration surface, in alloy 1. Color version available online.

B. *Precipitates in Alloy 2*

Next, we discuss the precipitates found in 580 MPa alloy 2 which has 0.07 Ti and 0.034 Nb (at. pct). Figure 6 shows a portion of a (Ti,Nb)(C,N) precipitate captured. The figure shown is only to illustrate the size scale of the precipitate, whereas the focus is on identifying the composition of the precipitate. We have obtained the composition of the precipitate in two ways: (1) by isolating 3 nm^3 volume from three different areas within the precipitate and averaging the composition from each of these volumes and (2) by isolating the complete precipitate volume in the reconstruction. The average composition of the 3 nm^3 cube volume is 33.79 ± 1.11 Ti, 26.55 ± 1.03 Nb, 33.63 ± 1.11 C, 6.02 ± 0.55 N (at. pct) and that of the whole precipitate is 30.32 ± 0.38 Ti, 26.33 ± 0.33 Nb, 35.08 ± 0.44 C, 8.26 ± 0.12 N (at. pct). Composition details are listed in

Table IV. Precipitate Composition (At. Pct) in Alloy 1 Obtained From the Region Encompassed by 25 At. Pct Ti Isoconcentration Surface

	(Ti,Nb)(C)	(Ti,Nb)(C) Star-Shaped
Ti	48.55 ± 0.47	47.60 ± 0.20
Nb	12.18 ± 0.31	17.05 ± 0.15
C	39.26 ± 0.45	35.33 ± 0.19

The error of concentration c is defined as $\sigma = (c(1-c)/N)^{0.5}$, where N is the total number of detected ions used for calculating the concentration value.

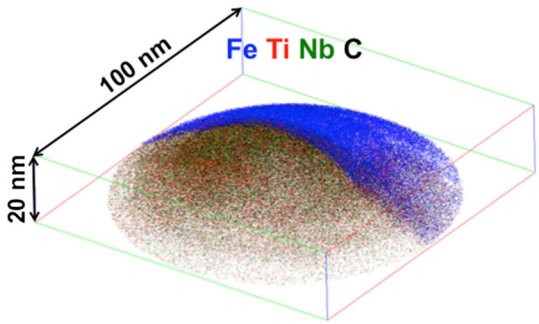

Fig. 6—(Ti,Nb)(C,N) precipitate in alloy 2. Only a portion of this precipitate was captured. Color version available online.

Table V. Composition (At. Pct) From the Region Encompassed by the Carbo-Nitride Precipitate in Alloy 2

	(Ti,Nb)(C,N)
Ti	30.32 ± 0.38
Nb	26.30 ± 0.33
C	35.08 ± 0.44
N	8.26 ± 0.12

The error of each concentration c is defined as $\sigma = (c(1-c)/N)^{0.5}$, where N is the total number of detected ions used for calculating the concentration value.

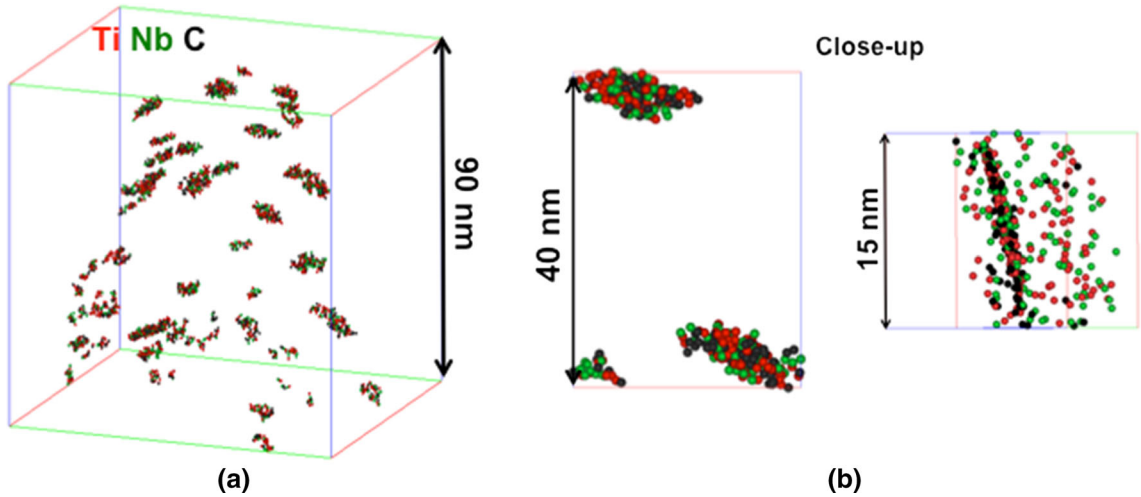

Fig. 7—(*a*) (Ti,Nb)(C) clusters found in alloy 2 with (*b*) showing a close-up of the clusters. Color version available online.

Table V. This is consistent with the composition obtained from 1D profile taken along the precipitate.

No (Ti,Nb)(C) precipitates, of a size similar to those observed in alloy 1, were found in alloy 2. When one considers the aggregate APT volumes analyzed—~300 nm × 300 nm × 50 nm for alloy 1 and ~390 nm × 390 nm × 50 nm for alloy 2—alloy 1 has ~12 times more (Ti,Nb)(C) precipitates than alloy 2. This difference in the precipitates is thought to be due to the difference in bulk alloy chemistry and is discussed in the context of thermodynamic calculations in Section IV–D. However, uniformly distributed GP-zone-like (Ti,Nb)(C) clusters were found in alloy 2, Figure 7. The composition of these clusters, analyzed using cluster analysis, was 33.79 ± 8.02 C, 38.40 ± 10.34 Ti, and 27.81 ± 6.84 Nb (at. pct). Reported uncertainity represents a standard deviation calculated from the composition of all the clusters in the reconstruction. Figure 7(b), close-up of these clusters, shows that they are only a few atomic layers thick, consistent with other studies where these monoatomic thick clusters are identified as GP-zone-like clusters[17,26,41] and their shape is thought to be more energetically favorable for nucleation.[26] This lack of large (Ti,Nb)(C) is consistent with observations in STEM–HAADF images and also with a few other experimental results.[17]

IV. DISCUSSION

The presence of multiple microalloying elements in a steel can effect the individual element's solubility and the precipitation events, which in turn control the microstructure. APT results provide accurate composition to understand the solute distribution among and within the precipitate and reconstruct the precipitation sequence. Our discussion will first reconstruct the precipitate sequence and then discuss the composition and the precipitation events in the two steels.

A. *Precipitation Sequence in Alloy 1 and Alloy 2*

To understand the precipitation sequence, we performed thermodynamic calculations for alloy 1 and 2 and the results are plotted in Figure 8. Two important conclusions were noted—First, as seen in Figures 8(a) and (b), carbo-nitride precipitates begin to form at a higher temperature followed by carbide precipitates in both alloys. Second, as seen in Figure 8(c), carbo-nitride precipitates that nucleate at a higher temperature are rich in Ti (not shown here) and N, but lean in C. The next precipitate layer to nucleate at a lower temperature will be a solid solution of Ti, N, and C and its composition will depend on the temperature at which it nucleates. However, it will have less N and more C than the precipitate layer on which it nucleates. As the temperature decreases continuously, each successive precipitate layer that heterogeneously nucleates onto an already-precipitated TiN-rich core will become progressively richer in C and leaner in N, shown schematically in Figure 8(c). As the temperature is further decreased, the amount of N in these layers is reduced until it is exhausted from the matrix. We suggest that N is completely exhausted because our experimental APT results showed no dissolved N in the matrix in any of the atom probe experiments. As the temperature continues to decrease, Nb will start to precipitate as NbC onto the TiN-rich core which will result in the outer precipitate layers being richer in Nb. This description will result in a carbo-nitride precipitate, which grows by acting as a nucleation site, and has multiple layers associated with a different solid solution composition heterogeneously nucleating at each temperature.

Once N is depleted, two precipitation events are possible. First, (Ti,Nb)(C) will continue to nucleate on the existing carbo-nitride precipitates, and second independent precipitation of (Ti,Nb)(C) will occur in the matrix or on lattice defects. The independent carbide precipitation event will also occur in a similar manner but with a TiC-rich core. Perez *et al*. have noted distinct sets of NbN and Nb(C,N) precipitates which can be

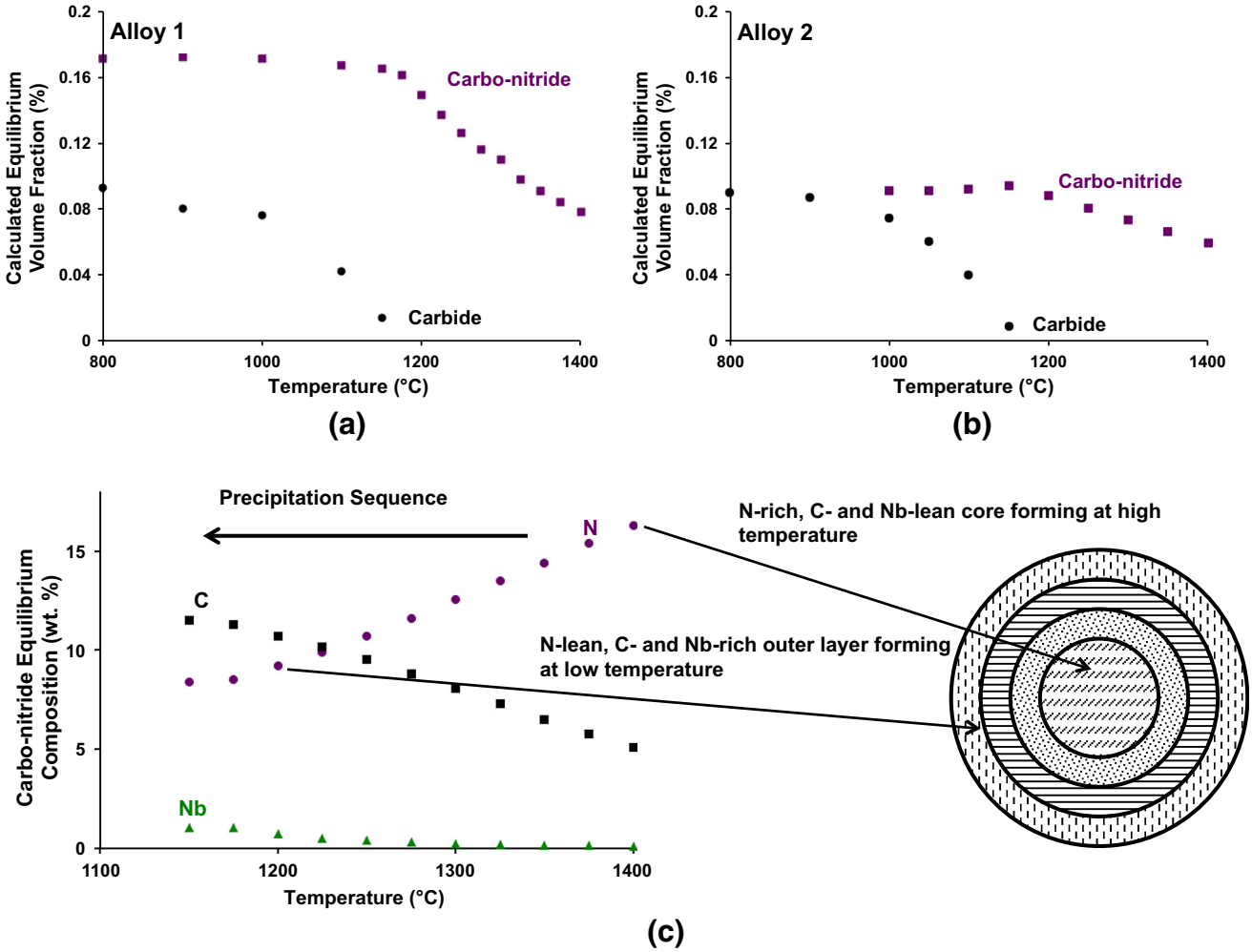

Fig. 8—Calculated volume fraction of (Ti,Nb)(C) and (Ti,Nb)(C,N) as a function of temperature in (*a*) alloy 1, and (*b*) alloy 2. (*c*) Composition of (Ti,Nb)(C,N) in alloy 1 as a function of temperature with the schematic illustrating the successive layers of varying composition forming as the alloy is cooled. Color version available online.

explained by the precipitation sequence proposed above.[21] Our deduction is also supported by the fact that the experimentally observed larger precipitates were carbo-nitride, Figure 4, suggesting that they nucleated at a higher temperature and had a longer time to grow, by acting as nucleation sites, as compared to the carbide precipitates. Similarly, it is reasonable to deduce that the smaller precipitates nucleated later in the precipitation sequence at a lower temperature. Therefore, the size of the precipitate is related to the temperature at which it nucleates. This proposed precipitation sequence is analogous to the core–shell composition observed in other steels.[11,19] For instance, Shanmugam *et al.* noted Ti, Nb, and V enriched in the cores and only Nb and V enriched in the shell. However, the observation of a distinct resolvable core–shell morphology will depend on the amount and the type of solutes and the processing temperature.

B. *Alloy 1: Nb Composition in the Precipitates*

The amount of Nb in the (Ti,Nb)(C) precipitates decreases from 10.90 to 1.54 (at. pct) or from 0.20 to 0.04 Nb/(Nb + Ti) as the size of the (Ti,Nb)(C) decreased. These composition values are obtained from the core of the precipitates, 1 nm from the interface, which should be minimally effected by evaporation field artifacts, if any.[42] This size-dependent composition is explained by Nb supersaturation in the matrix at the nucleation temperature of these precipitates. As mentioned in Section IV–A, precipitate size is related to the nucleation temperature—the larger precipitates nucleate at a higher temperature and grow by acting as a nucleation site for the precipitates that form later in the sequence and are rich in Nb. Therefore, the larger precipitates will have more Nb-rich layers and therefore a higher amount of Nb. This removal of Nb from the

matrix continuously lowers Nb supersaturation in the matrix. Consequently, the smaller precipitates that form at a lower temperature are relatively Nb lean compared to the larger precipitates that form earlier in the sequence.

C. *Alloy 1: Fe in the (TiNb)(C) Precipitates*

We now address the presence of Fe in the smaller (Ti,Nb)(C) precipitates. The (Ti,Nb)(C)-medium and (Ti,Nb)(C)-large, Figure 2(a) and (b), had no appreciable Fe dissolved in them, while (Ti,Nb)(C)-small had an appreciable amount of Fe. To demonstrate the size effect on the amount of Fe in the precipitate, we compared two of the smaller precipitates' proxigram composition profiles, Figure 9, with only Fe, Ti, and C profiles shown. As the size of the precipitates decreased from 1.65 to 1.00 nm, the Fe in the precipitate increased from 63.23 ± 1.31 to 81.72 ± 1.22 (at. pct). To alleviate concerns that the presence of Fe could be due to trajectory aberrations, the reported composition values are from 1 nm away from the precipitate/matrix interface.[42] Moreover, recent work on Nb(C,N) nano-precipitates has shown that the Fe matrix ions did not suffer from severe trajectory aberrations.[32] Therefore, it is unlikely that the presence of Fe is an artifact. Danoix *et al.* have reported Fe dissolved in analogous precipitates,[26] and inferred that Fe reduces the lattice misfit and makes it easier for the precipitate to nucleate. Similar Fe-containing metastable precipitates in steels have been observed experimentally and predicted by first-principles computation.[34,35,39] These studies have established that the presence of Fe helped stabilize the precipitates and makes their nucleation easier. Therefore, we hypothesize that Fe plays a similar role in (Ti,Nb)(C)-small precipitates.

D. *Precipitation and Clustering Behavior in Alloy 1 and 2*

Nine precipitates were found after studying 20 samples, approximately 300 nm × 300 nm × 50 nm, in alloy 1. A portion of a large precipitate was found in alloy 2 after studying 45 samples, approximately 390 nm × 390 nm × 50 nm. This suggests that alloy 1 has ~10 to 12 times more precipitates than alloy 2. However, alloy 2 did have uniformly distributed GP-zone-like (Ti,Nb)C clusters. To enable us to discuss the results quantitatively, the precipitates are examined in terms of number density calculated based on the collective volume of all the samples studied (Table VI).

The lack (low number density) of larger (Ti,Nb)-based complex precipitates in alloy 2 can be explained by the bulk composition and the precipitation sequence. Alloy 2 has approximately half the amount of Ti than alloy 1. Elaborating on the precipitation sequence among the complex precipitates, the TiN-rich complex precipitates will begin to form first at higher temperatures. Both alloys have the same amount of N and are hyperstoichiometric with respect to Ti for the formation of TiN. This means that an equivalent amount of Ti will be used in the formation of TiN and subsequently

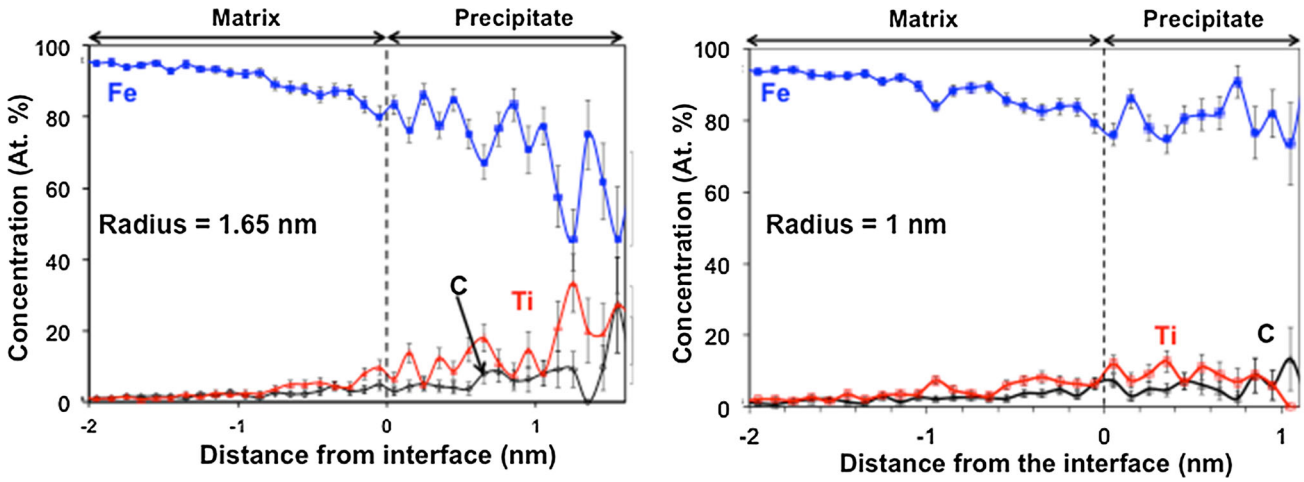

Fig. 9—Proximity histogram concentration profiles (At. Pct) of Fe, Ti, and C for (Ti,Nb)(C) precipitates obtained from 5.5 At. Pct Ti isoconcentration surface in alloy 1. The total number of detected ions in the precipitate portion of the proxigram is 1360 and 1240, respectively. Color version available online.

Table VI. Number Density (Precipitates/m^3) of (Ti,Nb)(C) and (Ti,Nb)(C,N) Precipitates in Alloy 1 and Alloy 2, as Measured by APT

Carbides (Ti,Nb)(C)		Carbo-nitrides (Ti,Nb)(C,N)	
Alloy 1	Alloy 2	Alloy 1	Alloy 2
$(1.52 \pm 0.57) \times 10^{21}$	At least $<0.13 \times 10^{21}$	2.17×10^{20}	9.33×10^{19}

The error for number density is based on counting statistics.

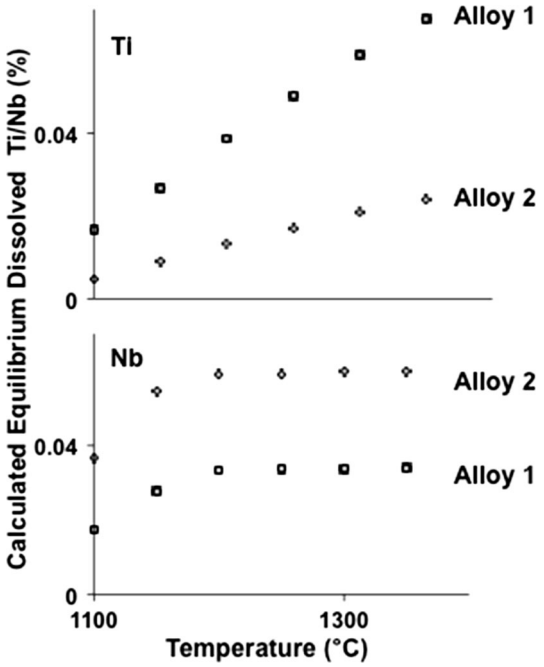

Fig. 10—Ti and Nb dissolved in the matrix as a function of temperature in alloy 1 and alloy 2.

(Ti,Nb)(C,N). However, alloy 2 has half the amount of Ti resulting in a lower amount of Ti in the matrix (supersaturation) after the TiN and (Ti,Nb)(C,N) precipitates have formed. Thermodynamic calculations performed in Thermo-Calc, Figure 10, are consistent with this hypothesis and show that alloy 2 will have a lower Ti amount in the matrix after the (Ti,Nb)(C,N) has formed. Even though there is some uncertainty at what exact temperature the carbides nucleate, the general trends in Figure 10 consistently show a lower amount of dissolved Ti and a higher amount of dissolved Nb in the matrix for alloy 2. This observation—no large precipitates but instead the formation of GP-zone-like clusters—has also been reported in other hot-rolled steels with only Nb.[17,22,41]

V. CONCLUSIONS

1. Nine precipitates were found after studying 20 samples, totaling approximately 300 million ions, in alloy 1. A portion of a large precipitate was found in alloy 2 after studying 45 samples, totaling approximately 500 million ions. This suggests that alloy 1 has approximately 10 to 12 times more precipitates than alloy 2 and this is attributed to the higher amount of Ti in alloy 1. Alloy 2 also had uniformly distributed GP-zone-like (Ti,Nb)(C) clusters.
2. In high-Ti alloy 1, Ti-rich carbo-nitride and carbide precipitates were observed. Carbo-nitride (Ti,Nb)(C,N) precipitate was measured to be approximately 40 nm × 40 nm × 10 nm. Carbide (Ti,Nb)(C) precipitates ranged from small spherical precipitates ~1.5 nm radius to elliptical/cuboidal precipitates that measured approximately 16 nm × 13 nm × 8 nm in size. In the high-Nb alloy 2, carbo-nitride (Ti,Nb)(C,N) precipitate was observed and no carbide (Ti,Nb)(C) precipitates were observed. Instead, uniformly distributed (Ti,Nb)(C) GP-zone-like clusters were observed.
3. Based on the experimental results and thermodynamic calculations, the precipitation sequence in both the alloys is rationalized as follows: carbo-nitride precipitates nucleate at a higher temperature and are rich in Ti and N but lean in C. As the temperature decreases, successive (Ti)(C,N) precipitate layers nucleate onto already-precipitated TiN-rich cores. As the temperature is decreased, these precipitate layers became progressively richer in C and leaner in N until eventually N is exhausted from the matrix. Eventually, Nb will also start precipitating in the outer layers and the outer precipitate layers become richer in Nb. Once N is depleted, a second set of (Ti,Nb)(C) will precipitate in a similar manner in the matrix or on lattice defects, in addition to precipitating onto the carbo-nitrides.
4. The amount of Nb in the precipitates decreases with the size of the precipitate—from 0.20 to 0.04 Nb/(Nb + Ti) . This was explained based on the amount of Nb in the matrix at the nucleation temperature. The precipitates (carbide or carbo-nitride) that nucleated at a higher temperature earlier in the sequence will be larger because they grow by acting as nucleation sites for phases that formed at lower temperatures and are rich in Nb. Consequently, the larger precipitates will have more Nb-rich layers. This removal of Nb from the matrix continuously lowers Nb supersaturation in the matrix. Consequently, the smaller precipitates that form at a lower temperature are relatively Nb lean compared to the larger precipitates.
5. In high-Ti alloy 1, a star-shaped/cruciform precipitate with a higher amount of Nb, 0.26 Nb/(Nb + Ti), than that in the other precipitates was observed. This precipitate, in addition to the other larger precipitates, retains Nb making this element less available for subsequent low-temperature precipitation. This is reflected in the absence of experimentally observed (Ti,Nb)(C) GP-zone-like solute clusters.
6. In the high-Ti alloy 1, the amount of Fe in the core of the (Ti,Nb)(C)-small precipitate increased as the size of the precipitate is decreased. This dissolved Fe is thought to make it easier for the precipitate to nucleate.

ACKNOWLEDGMENTS

The authors would like to acknowledge the Alabama Innovation Grant for their support. UA's Central Analytical Facility operated under the Office for Sponsored Research is also acknowledged. Ms. Suzanne

Kornegay and Mr. Tyler Kaub are acknowledged for their assistance in obtaining STEM–HAADF images and XRD scans, respectively.

ELECTRONIC SUPPLEMENTARY MATERIAL

The online version of this article (doi:10.1007/s11661-016-3398-6) contains supplementary material, which is available to authorized users.

REFERENCES

1. T. Gladman: *The Physical Metallurgy of Microalloyed Steels*, Maney, London, 2002.
2. M.P. Rao, V.S. Sarma, and S. Sankaran: *Mater. Sci. Eng. A*, 2013, vol. 568, pp. 171–75.
3. M. Charleux, W.J. Poole, M. Militzer, and A. Deschamps: *Metall. Mater. Trans. A*, 2001, vol. 32A, pp. 1635–47.
4. E. Pereloma, I. Timokhina, K. Russell, and M. Miller: *Scripta Mater.*, 2006, vol. 54, pp. 471–76.
5. I.B. Timokhina, P.D. Hodgson, S.P. Ringer, R.K. Zheng, and E.V. Pereloma: *Scripta Mater.*, 2007, vol. 56, pp. 601–04.
6. H.-W. Yen, P.-Y. Chen, C.-Y. Huang, and J.-R. Yang: *Acta Mater.*, 2011, vol. 59, pp. 6264–74.
7. R. Misra, K. Tenneti, G. Weatherly, and G. Tither: *Metall. Mater. Trans. A*, 2003, vol. 34A, pp. 2341–51.
8. A. Ruiz-Aparicio. Evolution of Microstructure in Nb-Bearing Microalloyed Steels Produced by the Compact Strip Production Process. Masters Thesis, Material Science and Engineering University of Pittsburgh, 2004, pp. 154.
9. S. Shanmugam, M. Tanniru, R.D.K. Misra, D. Panda, and S. Jansto: *Mater. Sci. Technol.*, 2005, vol. 21, pp. 883–92.
10. M. Tanniru, S. Shanmugam, R.D.K. Misra, D. Panda, and S. Jansto: *Mater. Sci. Technol.*, 2005, vol. 21, pp. 159–64.
11. S. Shanmugam, M. Tanniru, R. Misra, D. Panda, and S. Jansto: *Mater. Sci. Technol.*, 2005, vol. 21, pp. 165–77.
12. C.P. Reip, S. Shanmugam, and R.D.K. Misra: *Mater. Sci. Eng. A*, 2006, vol. 424, pp. 307–17.
13. Z. Jia, R.D.K. Misra, R. O'Malley, and S.J. Jansto: *Mater. Sci. Eng. A*, 2011, vol. 528, pp. 7077–83.
14. Y. Li, D.N. Crowther, P.S. Mitchell, and T.N. Baker: *ISIJ Int.*, 2002, vol. 42, pp. 636–44.
15. R. Wang, C.I. Garcia, M. Hua, K. Cho, H. Zhang, and A.J. DeArdo: *ISIJ Int.*, 2006, vol. 46, pp. 1345–53.
16. Y. Li, J.A. Wison, D.N. Crowther, P.S. Mitchell, A.J. Craven, and T.N. Baker: *ISIJ Int.*, 2004, vol. 44, pp. 1093–1102.
17. K.Y. Xie, L. Yao, C. Zhu, J.M. Cairney, C.R. Killmore, F.J. Barbaro, J.G. Williams, and S.P. Ringer: *Metall. Mater. Trans. A*, 2011, vol. 42A, pp. 2199–2206.
18. P.J. Felfer, C.R. Killmore, J.G. Williams, K.R. Carpenter, S.P. Ringer, and J.M. Cairney: *Acta Mater.*, 2012, vol. 60, pp. 5049–55.
19. T. Baker, Y. Li, J. Wilson, A. Craven, and D. Crowther: *Mater. Sci. Technol.*, 2004, vol. 20, pp. 720–30.
20. R.D.K. Misra, H. Nathani, J.E. Hartmann, and F. Siciliano: *Mater. Sci. Eng. A*, 2005, vol. 394, pp. 339–52.
21. M. Perez, E. Courtois, D. Acevedo, T. Epicier, and P. Maugis: *Philos. Mag. Lett.*, 2007, vol. 87, pp. 645–56.
22. Y. Chen, G. Tang, H. Tian, L. Feipeng, Y. Zhang, L. Wang, Z. Deng, and D. Luo: *J. Mater. Sci. Technol.*, 2006, vol. 22, pp. 759–62.
23. A. Craven, K. He, L. Garvie, and T. Baker: *Acta Mater.*, 2000, vol. 48, pp. 3857–68.
24. A. Craven, K. He, L. Garvie, and T. Baker: *Acta Mater.*, 2000, vol. 48, pp. 3869–78.
25. C.M. Enloe, K.O. Findley, C.M. Parish, M.K. Miller, B.C. De Cooman, and J.G. Speer: *Scripta Mater.*, 2013, vol. 68, pp. 55–58.
26. F. Danoix, E. Bémont, P. Maugis, and D. Blavette: *Adv. Eng. Mater.*, 2006, vol. 8, pp. 1202–05.
27. E. Bémont, E. Cadel, P. Maugis, and D. Blavette: *Surf. Interface Anal.*, 2004, vol. 36, pp. 585–88.
28. S. Mukherjee, I.B. Timokhina, C. Zhu, S.P. Ringer, and P.D. Hodgson: *Acta Mater.*, 2013, vol. 61, pp. 2521–30.
29. J. Angseryd, F. Liu, H.O. Andren, S.S. Gerstl, and M. Thuvander: *Ultramicroscopy*, 2011, vol. 111, pp. 609–14.
30. O.C. Hellman, J.A. Vandenbroucke, J. Rusing, D. Isheim, and D.N. Seidman: *Microsc. Microanal.*, 2000, vol. 6, pp. 437–44.
31. M.K. Miller: *Atom Probe Tomography: Analysis at the Atomic Level*, Springer, New York, 2012.
32. A.J. Breen, K.Y. Xie, M.P. Moody, B. Gault, H.-W. Yen, C.C. Wong, J.M. Cairney, and S.P. Ringer: *Microsc. Microanal.*, 2014, vol. 20, pp. 1100–10.
33. B. Gault, F. Danoix, K. Hoummada, D. Mangelinck, and H. Leitner: *Ultramicroscopy*, 2012, vol. 113, pp. 182–91.
34. M. Kapoor, D. Isheim, G. Ghosh, S. Vaynman, M.E. Fine, and Y.-W. Chung: *Acta Mater.*, 2014, vol. 73, pp. 56–74.
35. M.D. Mulholland and D.N. Seidman: *Acta Mater.*, 2011, vol. 59, pp. 1881–97.
36. J.J. Irani and R.W.K. Honeycombe: *J. Iron Steel Inst.*, 1965, vol. 203, pp. 826–33.
37. D. Raynor, J.A. Whiteman, and R.W.K. Honeycombe: *J. Iron Steel Inst.*, 1996, vol. 204, pp. 349–54.
38. D.H. Jack and K.H. Jack: *Mater. Sci. Eng.*, 1973, vol. 11, pp. 1–27.
39. J.H. Jang, C.-H. Lee, Y.-U. Heo, and D.-W. Suh: *Acta Mater.*, 2012, vol. 60, pp. 208–17.
40. W.-B. Lee, S.-G. Hong, C.-G. Park, and S.-H. Park: *Metall. Mater. Trans. A*, 2002, vol. 33A, pp. 1689–98.
41. K.Y. Xie, T. Zheng, J.M. Cairney, H. Kaul, J.G. Williams, F.J. Barbaro, C.R. Killmore, and S.P. Ringer: *Scripta Mater.*, 2012, vol. 66, pp. 710–13.
42. F. Vurpillot, A. Bostel, and D. Blavette: *Appl. Phys. Lett.*, 2000, vol. 76, pp. 3127–29.